Heliyon 10 (2024) e33360

Contents lists available at ScienceDirect

Heliyon

journal homepage: www.cell.com/heliyon

Research article

Ferromagnetic ZnO nanostructures from an organo zinc complex formulated via Piper Longum L-assisted green synthesis: Multifaceted prospects in photocatalysis, antimicrobial activity, and cell viability studies

Daphne Mary John [a,b], Nilesh S. Pillai [a,b], Akshay Sivan [a,b], Lasya P [a,b], Archana P [b,c], K.M. Sreekanth [a,b,**], Sivasubramanian G [b,c,***], Sreedhar K.M [d,*]

[a] Department of Physics, Amrita School of Physical Sciences, Coimbatore, Amrita Vishwa Vidyapeetham, India
[b] Advanced Multi-Functional Materials and Analysis Laboratory (AMMAL), Amrita School of Engineering, Coimbatore, Amrita Vishwa Vidyapeetham, India, 641112
[c] Department of Chemistry, Amrita School of Physical Sciences, Coimbatore, Amrita Vishwa Vidyapeetham, India
[d] Department of Chemistry, Amrita Vishwa Vidyapeetham, Amritapuri, Kerala, India, 690525

ARTICLE INFO

Keywords:
Metal oxides
Green synthesis
Photocatalysis
Ferromagnetism
Drug degradation
Antibacterial property

ABSTRACT

Transition metal oxides like ZnO nanostructures are pivotal in various scientific and technological fields due to their chemical stability, high electrochemical coupling efficiency, and broad radiation absorption spectrum. This study offers an in-depth examination of ZnO nanostructures synthesized via the green route using Piper Longum L, emphasizing their photocatalytic efficacy in degrading organic pollutants such as Sulphanilamide and Chromium. The ZnO nanostructures with a rod-like morphology exhibited an average crystallite size of 26 nm and an optical bandgap of 2.8 eV. Solid state structure of ZnO was investigated by Fourier Transform Infrared spectroscopy (FTIR) and X-Ray Diffraction (XRD). Zinc in the synthesized organo zinc complex and zinc oxide was estimated to 324.325 and 133.02 ppm, respectively. The saturation magnetization obtained from Superconducting Quantum Interference Device-Vibrating Sample Magnetometer (SQUID-VSM) for organo zinc complex and ZnO is 2.1×10^{-3} and 1.7×10^{-3} emu/g, respectively. These nanostructures achieved 99 and 93 % degradation of chromium (VI) ions present in solutions of two different concentrations in about 30 and 80 min, respectively, under UV and visible radiation, a remarkable achievement. Almost the same efficiency was maintained during three consecutive runs and then deactivation of the catalyst was observed. Additionally, a rapid 84 % degradation of Sulphanilamide was observed in 42 min, underscoring the potential of ZnO nanostructures as efficient photocatalysts for environmental remediation.

* Corresponding author.
** Corresponding author.
*** Corresponding author.
E-mail addresses: km_sreekanth@cb.amrita.edu (K.M. Sreekanth), g_sivasubramanian@cb.amrita.edu (S. G), sreedharkm@am.amrita.edu (S. K. M).

https://doi.org/10.1016/j.heliyon.2024.e33360
Received 20 March 2024; Received in revised form 18 June 2024; Accepted 19 June 2024
Available online 21 June 2024

1. Introduction

Semiconductors have always been an integral part of the nanoscience sector for multifunctional applications due to their compelling mechanical, thermal, magnetic, optoelectronic, and electrical properties. Semiconducting nanostructures include TiO_2, CuO, Al_2O_3, MnO, ZnO, etc, of which Zinc Oxide belonging to the semiconductor group II-VI proved to be the most beneficial one. Zinc oxide's flexibility stems from its unique physical and chemical properties [1–7]. Some of its attributes are high chemical stability, strong electrochemical coupling coefficient, broad spectrum of radiation absorption, and high photostability. It is appealing for prospective usage in electronics, optoelectronics, and laser technology due to its broad energy band (3.37 eV), high bond energy (60 meV), and robust thermal and mechanical stability at ambient temperature [8,9]. Cubic zinc blende and hexagonal wurtzite are the two most common forms of zinc oxide, with wurtzite being the most stable.

Green synthesis of nanoparticles has increased significant importance in recent years due to various advantages, including simplicity, cost-effectiveness, nanoparticle stability, reduced time consumption, non-toxic by-products, environmental friendliness, and the capacity to scale up for large-scale synthesis [10]. Plant extracts are easily obtainable and can act as stabilizing and reducing agents, an ideal technique for green synthesis of ZnO nanoparticles (NPs) [10]. This technique also has the additional advantage because plant-based nanoparticles' physio-chemical features extend the life span of NPs, which overcomes the limits of conventional chemical and physical NPs production methods [11]. Conventionally synthesized NPs have limited therapeutic application due to their toxicity. The antibacterial activity of ZnO NPs obtained using plant extracts is much higher than that of chemically synthesized ZnO NPs without antibiotic resistance. They are non-toxic and adaptable to the skin, making them suitable for use as additives in items that will encounter humans. Based on these properties, the green synthesis of ZnO NPs using plant extracts can be exploited to provide antibacterial activity to textiles, maintaining an ecologically friendly development. As a result, when ZnO NPs are added to finished fabrics in the textile industry, they exhibit UV and visible light resistance, antibacterial properties, and deodorant properties [12].

Many research articles are available in the public domain on the green synthesis of ZnO nanoparticles with the aid of plant extracts, for example, Ficus carica leaf extract, Moringa oliefera, Rubia cordifolia root extract, etc [13–15]. The advantage of the work lies in harvesting the bioactive molecules of Piper longum L in synthesizing an organo zinc complex, which has excellent antibacterial and antifungal properties. The biomolecules forming organo zinc complex can also act as capping agents, which prevent agglomeration, and sacrifice themselves at higher temperatures to yield nanostructures of ZnO [16]. ZnO nanostructures excavate independently into the domains of nutraceuticals, food supplements, zinc fortification, or high-end technological applications [17]. Piper plants are among the most important medicinal herbs in various medical systems. Piper longum (long pepper) is a flowering vine in the Piperaceae family cultivated for its fruit, which is used as a spice. Antifungal, insecticidal, antibacterial, antiamoebic, antidiabetic, antioxidant, anti-cancerous, and respiratory system effects are some of the pharmacological activities of Piper longum [18,19]. Plant extracts are easily obtainable, the method only requires a metal salt solution as a precursor [20]. Apart from its medicinal value, Piper longum L was not explored much on its application in generating zinc oxide as a photocatalyst.

This work focuses on a novel green route mechanism for synthesizing ZnO nanostructures using Piper Longum L to investigate its effect on degrading and reducing harmful contaminants commonly present in wastewater. Also, studying its structural, magnetic, thermal, optoelectronic, and biological properties to bring out its multifunctional characteristics and applications. The synthesized sample was subjected to different characterization techniques like X-ray diffraction to know its structure, morphological studies were done using SEM and elemental analysis by EDX and CHNS. UV–Vis. spectrum was taken to check for its band gap and to study the prepared ZnO's photocatalytic activity. The room temperature ferromagnetism was analyzed employing SQUID analysis, and the biological properties like antimicrobial activity and cytotoxicity are also interpreted in this paper.

2. Materials and methods

2.1. Chemicals utilized

High-purity chemicals were used for the synthesis. Sodium hydroxide pellets (NaOH, 97 % pure), acetone (C_3H_6O, 99 % pure), 30 % hydrogen peroxide solution (H_2O_2, 99 % pure), all from Avantor RANKEM, potassium dichromate ($K_2Cr_2O_7$, 99 % pure), and zinc nitrate hexahydrate ($Zn(NO_3)_2.6H_2O$, 96.0 % pure), all from EMPLURA. Export grade and dried Piper Longum L fruit, locally renowned as Thippali, was purchased from a trusted spice dealer at Tharecad village, Palakkad block, Palakkad district, Kerala, India. For preparing solutions and washing purposes, ASTM Type I deionized water was used.

2.2. Preparation of Piper Longum L fruit extract

The dried fruit was manually ground in a mortar. 10 g of the powder was transferred into a Whatman paper pouch and then subjected to Soxhlet extraction with ASTM Type I water.

2.3. Preparation of organo zinc complex

100 mL solution of 0.5 M $Zn(NO_3)_2$ was prepared in ASTM Type I water from 14.8 g of zinc nitrate hexahydrate and then added to 100 mL Piper Longum L fruit extract at room conditions of temperature and pressure. This solution was allowed to swirl at 800 rpm for 1 h, and then NaOH solution was added dropwise to ensure maximum precipitation of the organo zinc complex at about a pH of 6.9. Stirring was prolonged to 2 h and eventually, the solution turned pale yellow. A vacuum filtering procedure was used to separate the

organo zinc complex from the solution using a Whatman 41 filter paper. The precipitate thus obtained was heated to 100 °C for 2.30 h in a hot air oven to remove the water content to yield dry organo zinc complex.

2.4. Preparation of ZnO NPs

The dry organo zinc complex thus obtained was ground using a mortar to make it fine powder, which was then transferred to a crucible. It was kept in a muffle furnace for 4 h at 600 °C, resulting in a white compound, ZnO.

2.5. Characterization techniques

ZnO nanostructures were characterized by XRD (Bruker AXS D8 ADVANCE Diffractometer with Cu–K alpha radiation $\lambda = 1.5406$ Å) for phase identification. The surface morphologies were analyzed using FESEM (Carl Zeiss Germany, Gemini 300), and elemental composition by Energy Dispersive X-Ray Spectrometry (EDS), attached with FESEM. Thermogravimetric analysis (TGA) (TA Instruments, SDT Q600, USA) was done for pre-annealed and annealed samples to observe weight loss as a function of temperature. Absorption spectra of samples were grasped using UV–Vis. spectrometer (RITTUN UV-3660). FTIR (BRUKER ALPHA II, Germany) analyzed the functional groups present in the sample. CHNS elemental analyzer was exploited to qualitatively analyze carbon, hydrogen, nitrogen, and sulphur in the organo zinc complex. The quantification of the zinc in the obtained sample was analyzed using 884 professional VA | Metrohm. Magnetic properties of samples were characterized via SQUID analysis (MPMS-3 magnetometer Quantum Design).

2.6. Photocatalytic degradation of hexavalent chromium

Photocatalysis destroys organic pollutants effectively; yet, it has restricted usage of visible light, fast charge recombination, and low migratory ability of created electron-hole pairs, restricting its use in industrial environments. A fathom of research is being done to improve its applicability. Induced electrons and holes interact with oxygen (O_2), water (H_2O), and hydroxyl (OH) groups to generate reactive oxygen species (ROS) such as hydroxyl radicals and superoxide radical anions, which are responsible for the reduction [21, 22]. When the bandgap energy is large, the reaction is inhibited because the electrons and holes created recombine without participating in the process, resulting in a lower quantity of ROS formed on the surface that is accessible for photodegradation.

2.6.1. Preparation of 1, 5-diphenyl carbazide solution

1, 5-Diphenylcarbazide (DPC) functions as a redox and photometric indicator for heavy metal ions such as chromium, mercury, cadmium, osmium, rubidium, and technetium. DPC reacts with Cr (VI) ions in acid medium to form a violet solution, which is the foundation of this sensitive method. The cationic Cr (III)-diphenyl carbazone complex is formed due to the oxidation of diphenyl carbazide by Cr (VI) [23]. 0.25 g of 1, 5-diphenylcarbazide (Sigma Aldrich, 99.9 % purity) was dissolved in 50 mL acetone to make the reagent.

2.6.2. UV-assisted photocatalytic degradation of hexavalent chromium

Dissolving 0.106 g of potassium dichromate ($K_2Cr_2O_7$, Sigma Aldrich, 99 % purity) in deionized water yielded a 1000 ppm standard stock solution. To avoid deterioration, the stock solution was kept in the refrigerator. The stock solution was used to make working standards with concentrations of 100, and 200 ppm. 100 mL of 0.5 M oxalic acid solution was prepared from 6.3035 g of oxalic acid dihydrate salt (Sigma Aldrich, 99.9 % purity). 4 mL of 0.5 M oxalic acid was added to 20 mL of potassium dichromate working standard, which was stirred in the dark with 10 mg of synthesized ZnO. The stirred solution was subjected to UV-C assisted irradiation. A RITTUN UV-3660 double-beam UV–visible spectrophotometer with a 10 mm quartz cell was employed for Cr (VI) determination. Every 6 min, 1 mL of irradiated solution was pipetted out and was thoroughly mixed with 1 mL of DPC reagent. UV spectra were obtained for 1 mL of Cr (III)-diphenyl carbazone complex formed.

2.6.3. Visible light assisted photocatalytic degradation of hexavalent chromium

4 mL of 0.5 M oxalic acid was added to 20 mL of potassium dichromate working standard, which was mixed with 10 mg of synthesized ZnO under visible light. Every 15 min, 1 mL of irradiated solution was pipetted out and mixed with 1 mL of 1, 5-diphenylcarbazide reagent. The UV spectra of 1 mL of Cr (III)-diphenyl carbazone combination were obtained.

2.7. Photocatalytic degradation of sulphanilamide

Pharmaceuticals are created to enhance human health by treating ailments, but in the present scenario, it is considered as an emerging environmental contaminant, despite its importance to human and animal health [24]. The major issue faced due to the contamination of pharmaceuticals is their presence in the water bodies at lower concentrations. And because each of these compounds is chemically distinct, detecting, analyzing, and removing them from water and wastewater is challenging [25]. Therefore, degradation helps to identify the structure and the toxicity of the pharmaceuticals. Photocatalytic degradation of pharmaceuticals using a photocatalyst is a very cheap and more eco-friendly way. This helps to develop and validate stability. In this study, we are focusing on the degradation of Sulphanilamide ($C_6H_8N_2O_2S$). Sulphanilamide is an antibacterial drug. It is an organic molecule composed of aniline that has been derivatized with a sulfonamide group [25]. Sulphanilamide has been reported as an emerging organic pollutant

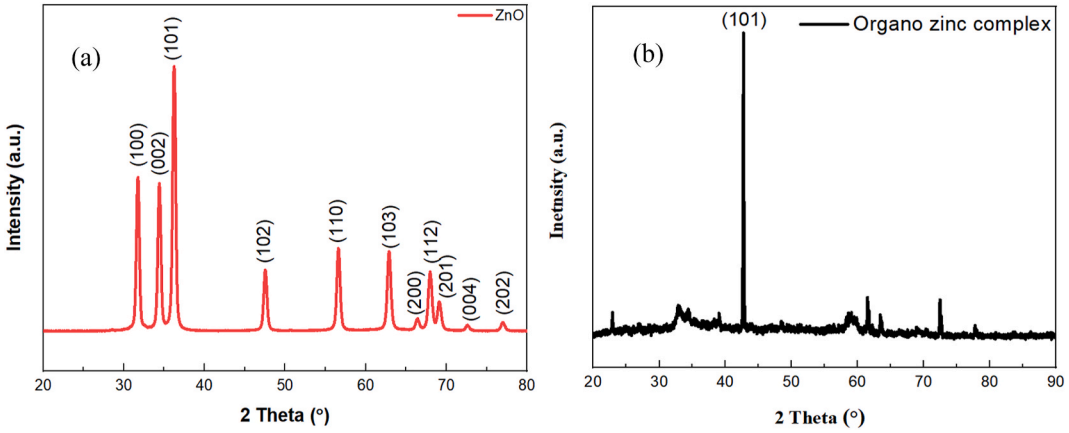

Fig. 1. XRD pattern of (a) synthesized ZnO and (b) organo zinc complex.

(EOCs) [26].

2.7.1. Methodology of photocatalytic degradation of sulphanilamide

10 ppm solution of Sulphanilamide was prepared. To dissolve completely, the solution was stirred for 15 min. The initial UV spectrum was measured. Then, the photocatalyst was added to the solution. The photocatalyst used here is the synthesized ZnO using Piper longum fruit extract. This was kept for 1 h stirring in dark to attain the absorption-desorption equilibrium. After 1 h of stirring, the solution was kept in a UV-C chamber. After every 6 min, 1 mL of the solution was pipetted out and UV–Vis. absorption spectrum of the solution was analyzed using the RITTUN UV-3660 UV–visible spectrophotometer. The absorption peak for Sulphanilamide was shown at 258 nm.

To check the reusability, the synthesized ZnO, which was used as a photocatalyst for the reduction of sulphanilamide, was washed using deionized water, and acetone and then dried. This used ZnO was added to a 10 ppm fresh solution of sulphanilamide. This was then kept for 1 h stirring in dark and then transferred to UV-C for reduction to happen. 1 mL of the solution was pipetted out in every 6 min and the UV spectrum was analyzed.

2.8. Preparation of Piper Longum L extract for phytochemical analysis

30 mL extract was taken from the stock, a working standard of 3 mL extract was transferred to test tubes, and tests were performed for qualitative analysis of Alkaloids, Flavonoids, Glycosides, Phenols, Saponins, Sterols and, Tannins.

2.9. Methodology of antimicrobial activity

The antibacterial activity was assessed using Well Diffusion technique at 37 °C for 24 h.

2.10. Toxicity analysis

For toxicity analysis, the MTT method was employed. The incubation period was 4 h at 37 °C in a 5 % CO_2 atmosphere. The MTT approach is simple, accurate, and yields reproducible results [27].

3. Results and discussion

3.1. Structure analysis

XRD was exploited to identify crystalline structure of synthesized materials. Cu K-alpha radiation, with a wavelength of 1.5406 Å, is widely used in X-ray diffraction (XRD) to probe the crystalline structure of solid minerals, allowing the determination of interplanar and interatomic distances. Fig. 1(a) depicts the diffraction pattern found for the synthesized nanoparticle, which was in identical match with ZnO nanoparticles (JCPDS File number 36–1451). For the 2θ value at 36.22°, the pattern showed a maximum intensity peak, which belongs to the plane (101).

The signals indicated the materials' crystalline composition. According to JCPDS data, the corresponding lattice planes are (100), (002), (101), (102), (110), (103), (200), (112), (201), (004), and (202), supporting the hexagonal wurtzite structure of the materials [28]. In XRD pattern of organo zinc complex as shown in Fig. 1(b), a sharp peak at 2 theta value of 43.4°, corresponding to (101) lattice plane, depicts the formation of zinc nanoparticles [29]. The decoction prepared from Piper Longum L has the potential to precipitate zinc from zinc nitrate solution, as is proven by the XRD pattern.

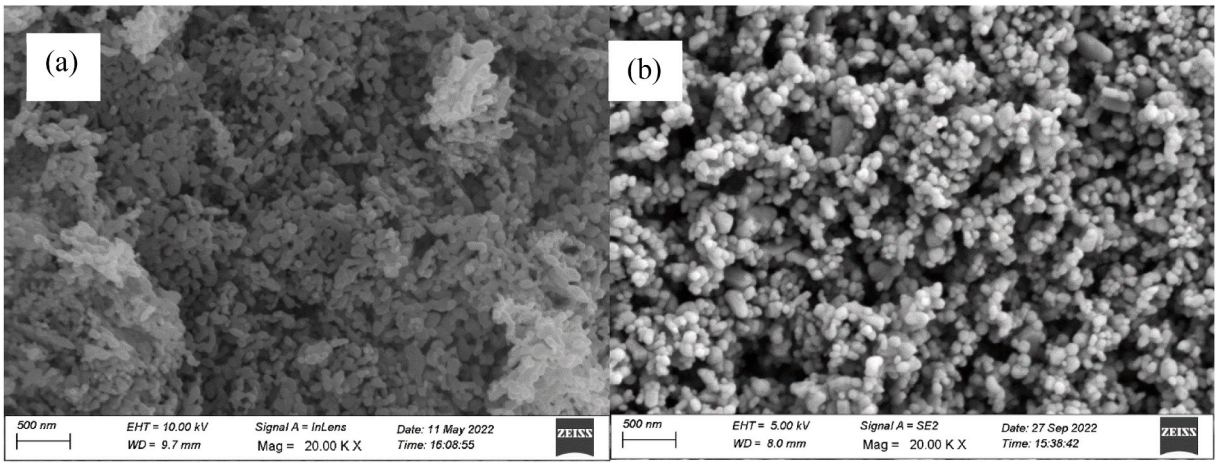

Fig. 2. SEM image of (a) green and (b) chemically synthesized ZnO NP at500 nm resolution.

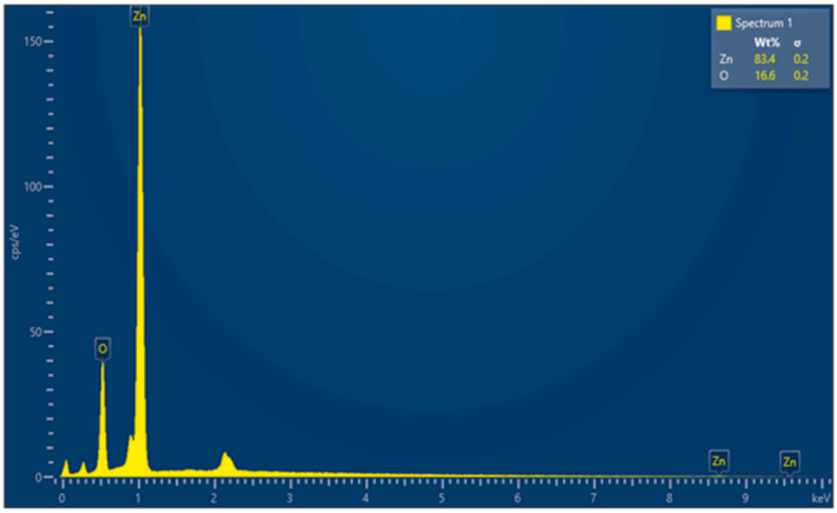

Fig. 3. EDX spectrum of synthesized ZnO NPs.

The Scherrer formula in equation (1) was used to compute the crystallite size, and the full-width half maxima were calculated from the plot using the (101) plane [30].

$$d = \frac{k\lambda}{\beta \cos\theta} \tag{1}$$

where, d is the average order size (crystalline), k is a dimensionless form factor with a value of 0.9, β is line widening half as strong as it might be (FWHM), and θ is the Bragg angle. The full width half maximum and crystallite size were determined, and the crystallite size was calculated to 17.9 and 14.8 nm for ZnO and organo zinc complex respectively.

3.2. Morphology and elemental analysis

The surface morphology of the resulting powder was studied with SEM, Fig. 2. Because of their small size and low aggregation, the green synthesized structures are constant in nature. Aggregation, which is likely owing to the high surface energy of ZnO-NPs formed during synthesis in an aqueous solution, is also seen, as is densification, which results in a tight spacing between particles [31]. The SEM image of the ZnO NPs generated displays a precise wurtzite hexagonal structure with smooth and well-defined contacting surfaces. The produced ZnO NP with an average particle size of 141 and 89 nm for green and chemically synthesized was identified from the analysis.

The cross-sectional rods have neither porous nor hollow morphology but are compact solid with no other morphologies at their neighboring rods. Nanorods join to produce ZnO grains with nearly homogeneous shape. The SEM image corresponding to green

Table 1
Composition of the prepared ZnO sample.

Element	Line Type	Apparent concentration	K Ratio	Wt %	Wt %	Atomic Wt %
O	K series	17.41	0.05857	16.61	0.17	44.87
Zn	L series	36.52	0.036521	83.39	0.17	55.13

Table 2
Inference from Phytochemical analysis.

Phytochemical	Test Name	Confirmation
Alkaloids	Iodine Test	Nil
Flavonoids	NaOH Test	Confirmed
Glycosides	Molisch's Test	Confirmed
Glycosides	Glycosides Test	Confirmed
Phenols	Phenol Test	Confirmed
Saponins	Foam Test	Confirmed
Tannins	Lead Acetate Test	Confirmed

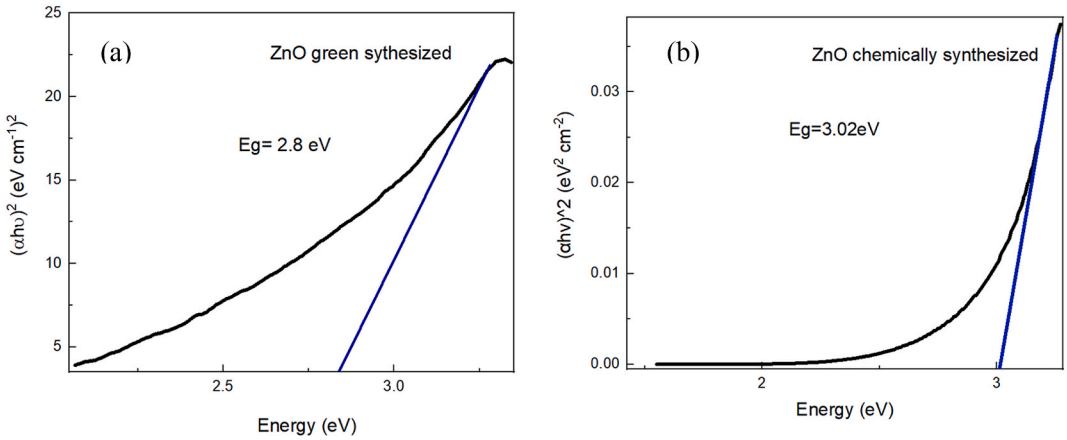

Fig. 4. Tauc plot for finding the energy band gap of (**a**) green and (b) chemically synthesized ZnO NPs

synthesized ZnO NP also shows tiny nanoparticles growing perpendicular to the surface. The confirmation of nanorods from SEM data, Fig. 2(a) added credence to the green synthesis approach. Thus, dried Piper Longum fruit-assisted synthesis is found an efficient and cost-effective way of growing nanorods than conventional method of getting sphere-like morphology, Fig. 2(b). From the EDS spectra in Fig. 3, the formation of ZnO can be confirmed and its composition is tabulated in Table 1.

3.3. Confirmation of phytochemicals

The qualitative analysis showed presence of the phytochemicals, Alkaloids, Flavonoids, Glycosides, Phenols, Saponins, Sterols, and Tannins in Piper Longum L extract and is shown in Table 2.

3.4. Optical analysis

3.4.1. UV spectra of synthesized sample

The UV spectrum of the synthesized sample displayed an absorbance peak like ZnO, indicating that the methodology utilized for green synthesis of ZnO NPs utilizing Piper Longum L fruit is successful. The sample was analyzed after 15 min of ultrasonication, which efficiently disseminated the material in deionized water. The spectrometer was allowed to run for one full cycle at wavelengths ranging from 200 to 800 nm. Intrinsic band-gap absorption of ZnO due to electron transitions from the valence band to the conduction band is seen in UV–visible absorption of ZnO NP as shown in Fig. 4.

The Tauc plot, Fig. 4 gives the value of the energy band as 2.8 and 3.02 eV for green and chemically synthesized ZnO NPs. As observed by SEM, the sample exhibits larger particle size, leading to a reduction in the band gap compared to the chemically synthesized ZnO of 3.02 eV. This decrease in the band gap may result from creating crystal defects such as oxygen vacancies in bigger crystallites [32]. EDX image, Fig. 3, quantifies the amount of oxygen as 44.87 %. Semiconducting ZnO contains intrinsic oxygen vacancy (Vo) defects. Higher oxygen vacancy concentrations can be induced in ZnO by annealing in an inert environment or oxygen

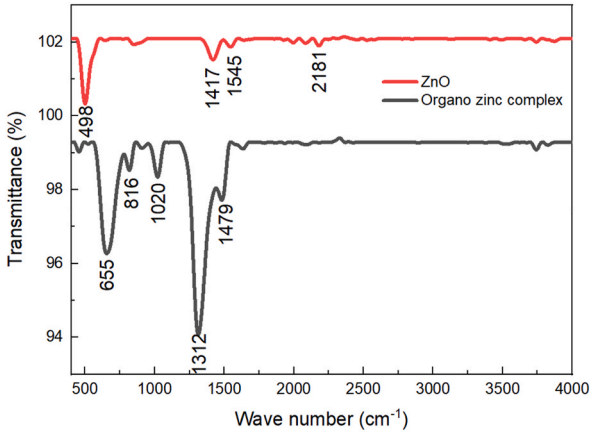

Fig. 5. FTIR spectra of synthesized ZnO and organo zinc complex.

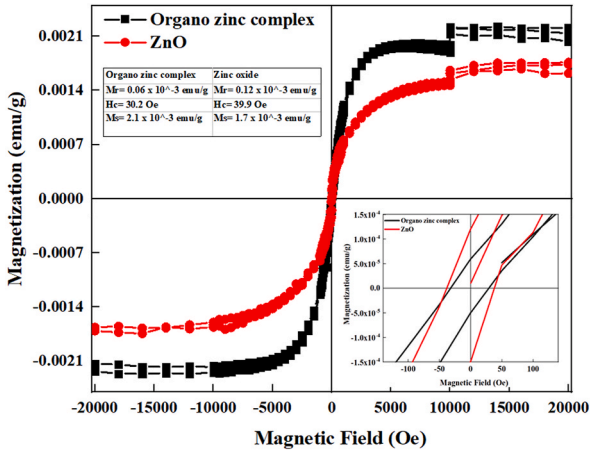

Fig. 6. Measurement of Magnetization (M) as a function of the Applied Magnetic Field (H) showing the hysteresis loop. Inset: Enlarged view of the hysteresis loop to highlight coercivity and remanence.

deficiency. The bandgap narrowing is due to oxygen vacancies [33].

3.4.2. FTIR spectra of synthesized ZnO

Different functional groups linked with the created zinc oxide nanoparticles were discovered using FTIR. From Fig. 5, where 2181, 1545, 1417, and 500 cm^{-1} are the absorption peaks in ZnO and for organo zinc complex, the peaks are 655, 816, 1020, 1312 and 1479 cm^{-1}. The absorption peak at 500 cm^{-1} represents Zn–O stretching. The bond between inorganic components is responsible for the band frequencies below 800 cm^{-1} [34]. The presence of different organic or inorganic species resulting from the synthesis process via the green route could be the reason for the peaks at 816, 1020, 1417 and 1479 cm^{-1}. Plant extracts or other biological components frequently utilized in green synthesis can leave behind organic residues that are detected in FTIR analysis. The peaks at 1417 and 1479 cm^{-1} are typically associated with bending vibrations of the CH_2 groups, 816 and 1020 cm^{-1} corresponds to C═C and C–N groups respectively, which could be remnants of the organic precursors used in the green synthesis of ZnO [34]. The peaks at 1312, 1545 and 2181 cm^{-1} could be due to surface contamination, absorbed species or functionalization of zinc oxide surface with organic molecules from the plant extracts [34].

3.5. Magnetic property analysis

3.5.1. SQUID analysis

The M − H loop for Zinc Oxide nanoparticle and organo zinc complex was obtained using SQUID-VSM. The experiment was conducted at a constant temperature and with a field range of ± 7 T and the diamagnetic characteristic is carefully removed from the loop. To ensure saturation magnetization, high applied field values were utilized, and the observed M − H loop of ZnO varied from that of organo zinc complex, as seen in Fig. 6. Organo zinc complex's magnetization curve, which showed little hysteresis, may be classified

Table 3
Elemental composition.

Sl. No.	Element	Content (%)
1	Carbon	2.261
2	Nitrogen	3.068
3	Hydrogen	1.600
4	Sulphur	0.065

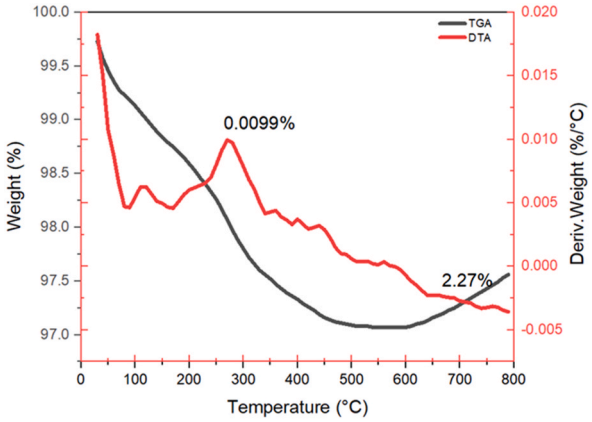

Fig. 7. TGA of zinc oxide.

as weakly ferromagnetic or superparamagnetic. The M − H curve of ZnO is inclined to be ferromagnetic. In a magnetic field of 16 kOe, organo zinc complex has a saturation magnetization, M_S of 2.1×10^{-3} emu/g, whereas zinc oxide has a less saturation magnetization, M_s of 1.7×10^{-3} emu/g. The increased M_S value indicates the enhanced ferromagnetism in organo zinc complex due to its smaller crystalline size, which may lead to single domain structures compared to zinc oxide, thereby enhancing its magnetic property. The decrease in the M_S value for zinc oxide might be due to the phase transformation induced during the heat treatment process, altering the crystal structure of the material, and affecting the magnetic interactions within the material in accordance with the XRD data discussed above.

High hysteresis, irreversible magnetization changes, and a shifted shape are visible, suggesting remanent magnetization (M_r) 0.12×10^{-3} emu/g for ZnO and 0.06×10^{-3} emu/g for organo zinc complex, respectively. ZnO has a coercivity (H_c) value of 39.9 Oe, whereas organo zinc complex has a value of 30.2 Oe. These results show that the synthesized ZnO has magneto-crystalline anisotropy and a good domain structure, also the smaller crystallite size of zinc oxide showed higher coercive value than organo zinc complex [35].

Squareness ratio is a valuable estimation of quality of magnetic materials and is given in equation (2). It measures how square is the hysteresis loop, provides information by which direction of magnetization reorients to the nearest easy axis magnetization direction after the magnetic field switch off [36].

$$Squareness\ ratio\ (SQR) = \frac{M_r}{M_s} \tag{2}$$

It should be as low as feasible for magnetic fluids. It should ideally be zero, due to structural formations (for example, chains); magnetization does not decrease to zero when the applied field is withdrawn [36]. A value of less than 0.5 denotes a modest single-domain, randomly oriented collection of spherical particles. Lower values are frequently related to bigger particles and the establishment of domain walls [36]. The SQR value of synthesized ZnO and organo zinc complex is 0.03 and 0.07, respectively. It has been known that neutral cation vacancies in simple binary oxides can give rise to holes on neighboring oxygen ions which give rise to a triplet ground state, which could be responsible for the ferromagnetism state in the metal oxides nanoparticles [37].

Nanorods with a high surface-to-volume ratio and proportionally more surface defects, as shown in SEM images Fig. 2, exhibit ferromagnetic behaviour. Because of the ongoing oxidation process on the surface of the nanorods, the nature of this ferromagnetic behaviour is unstable. Due to the high surface-to-volume ratio and intrinsic defects in ZnO nanostructures, a huge number of uncompensated surface spins are generated, giving rise to long-range ferromagnetic order. A defect complex linked with oxygen vacancy and the reduced cation can produce magnetic interaction [38]. Residual ferromagnetic impurities, which exist in the form of Zn interstitials and O vacancies, regulate ferromagnetic behaviour of ZnO Nanorods [36].

3.6. Validation of organo zinc complex

9.2810 mg of organic precipitate synthesized was used for CHNS analysis to confirm the occurrence of metal-containing organic compounds, the analysis quantified the presence of Carbon, Nitrogen, Hydrogen, and Sulphur, as shown in Table 3.

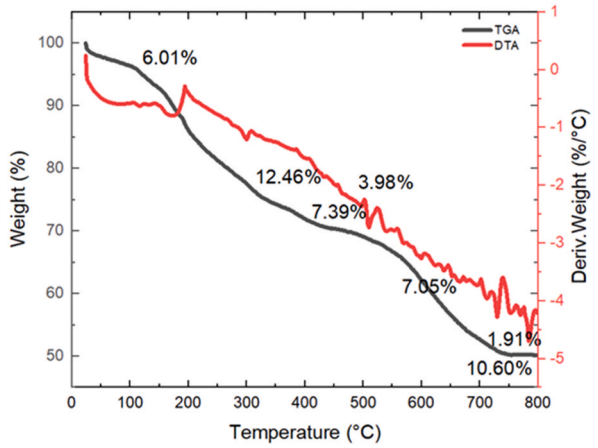

Fig. 8. TGA of organo zinc complex.

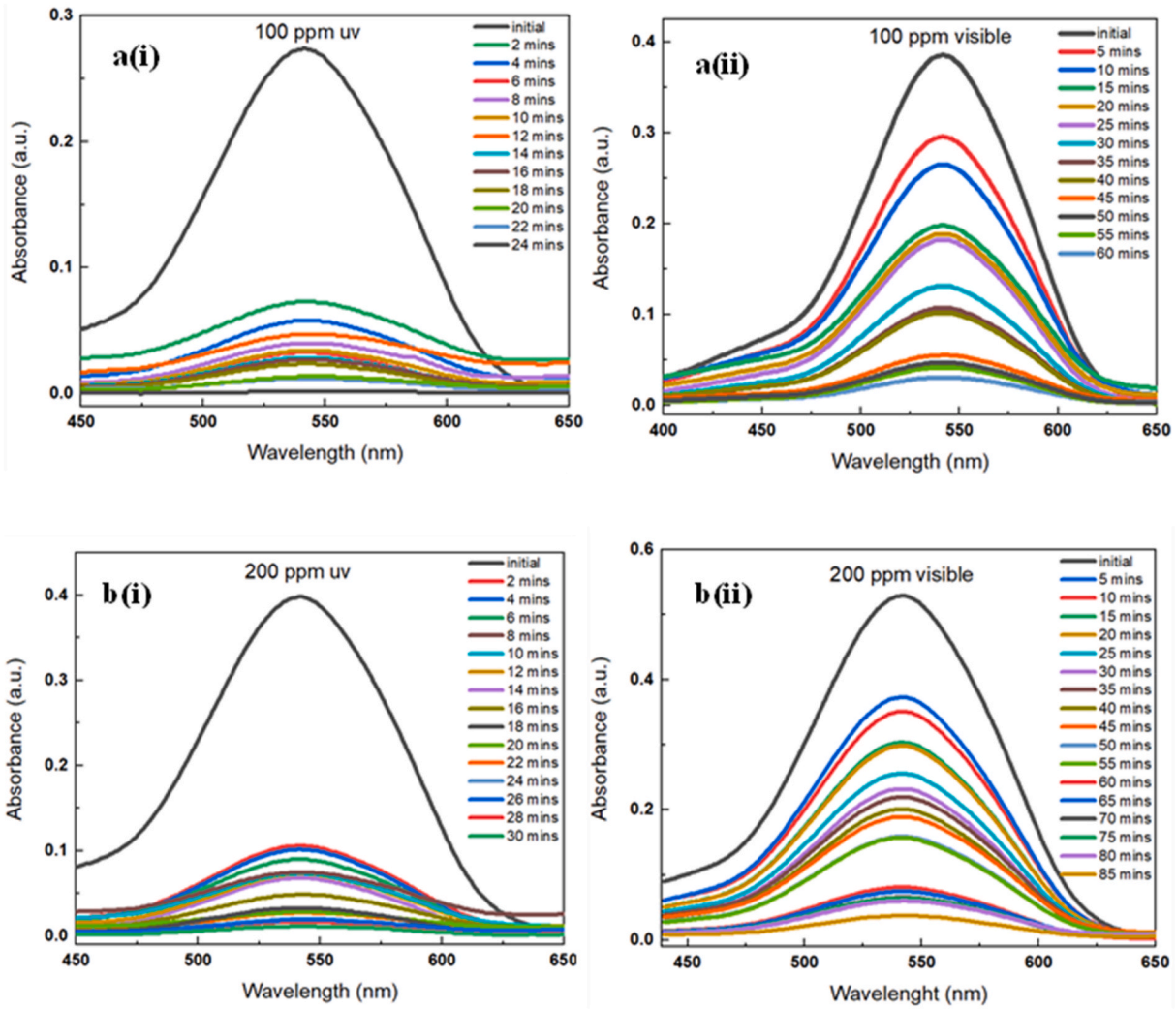

Fig. 9. Reduction in Chromium (VI) peak due to photocatalytic activity of synthesized ZnO, a(i) UV-C assisted, a(ii) LED assisted, 100 ppm and b(i) UV-C assisted, b(ii) LED, 200 ppm.

Table 4
Comparison of efficiency of synthesized catalyst in Cr (VI) reduction.

Photocatalyst	Radiation	Time (min)	Efficiency (%)	Reference
Synthesized ZnO	UV	24	99.6	Current study
Synthesized ZnO	Visible	60	91.6	Current study
ZnO (Nice)	UV	24	77.7	Current study
ZnO (Nice)	Visible	60	53.7	Current study
ZnO chemical route	UV	30	90	[42]
ZnO green route	UV	300	68	[43]
ZnO green route	UV	240	95	[44]

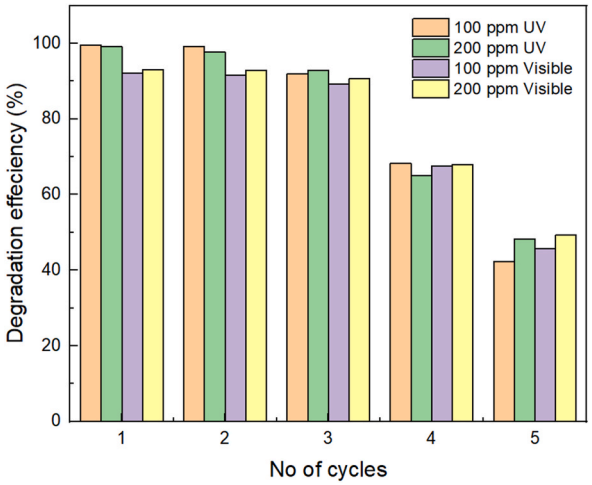

Fig. 10. The graph showing the reproducibility of ZnO photocatalyst for 5 cycles of activity.

The quantification of these compounds indicates the organic content in the precipitate formed. Using the 844 professional VA (Metrohm), the amount of Zn present in the digested sample of organo zinc complex is quantified.

In a 20 mL buffer solution of Sodium Acetate and Potassium Chloride, the presence of Zinc was not found in ppm level. The blank, also known as an acid combination (Hydrogen Peroxide and Nitric Acid), was used to aid digestion. 3.29 mg/L of zinc was found in a 0.5 g organo zinc complex sample. To achieve full homogenisation of the sample, the diluted organo zinc was treated to digestion in the microwave digestion system of the Multiwave GO Plus.

$$Conc. = \left[\, 884\ wieight\left(\frac{mg}{L}\right) - (blank + buffer) weight\ \left(\frac{mg}{L}\right)\right] \times \frac{dilutionvolume(L)}{weight\ of\ sample(kg)} \tag{3}$$

884 professional VA (Metrohm) determined that the sample has 133.02 ppm of Zinc using equation (3), indicating that the synthesized organo zinc complex contained 324.325 ppm of Zinc. When combined with CHNS data, the precipitate generated is verified to be an organic product with metal content.

3.7. Thermal analysis

The synthesized ZnO, and organo zinc complex were subjected to TGA analysis. The samples were heated at 20 °C/min in open DSC TG pans in a nitrogen atmosphere from 0 °C to 800 °C. Fig. 7 depicts the TGA of ZnO NPs. The TGA profile revealed a continual weight reduction with one near-sharp shift at 271.02 °C, followed by a near-constant plateau. Annealing at temperatures over 600 °C appears to ensure the creation of stable ZnO NPs. Excess water appears to be pushed out after heating to 271.02 °C, and the substance begins organic carbon breakdown. The substance is still decomposing, resulting in mass fluctuations and at 800.87 °C, the total weight loss remained 2.74 %. The TGA curve shows that sample be entirely degraded to ZnO after annealing at 800 °C.

The TGA demonstrated a five-stage weight loss in the case of organo zinc complex, as shown in Fig. 8, indicating the breakdown and vaporisation of distinct functional groups at varying temperatures. The considerable weight loss may be due to the breakdown of organic carbon coordinated with Zn. The initial dip at 100 °C marks vaporisation of water moisture, resulting in a 6 % reduction in mass changes [39]. It should be noted that the observed TGA shows that weight loss proceeds in successive stages with increasing temperature, which is the reduction of 6.994 % of organic content estimated in the sample from CHNS analysis. The first stage occurs between 50 °C and 120 °C, illustrating the dehydration of surface-adsorbed water. The second stage exhibits significant weightlessness between 190 °C and 320 °C, with weight loss of 10 % up to 600 °C, indicating the loss of OH^- and CO_3^{2-} [40]. The decomposition of organic molecules and oxygen in the sample resulted in considerable weight loss, as seen in the image (Fig. 8). The TGA curve reveals a

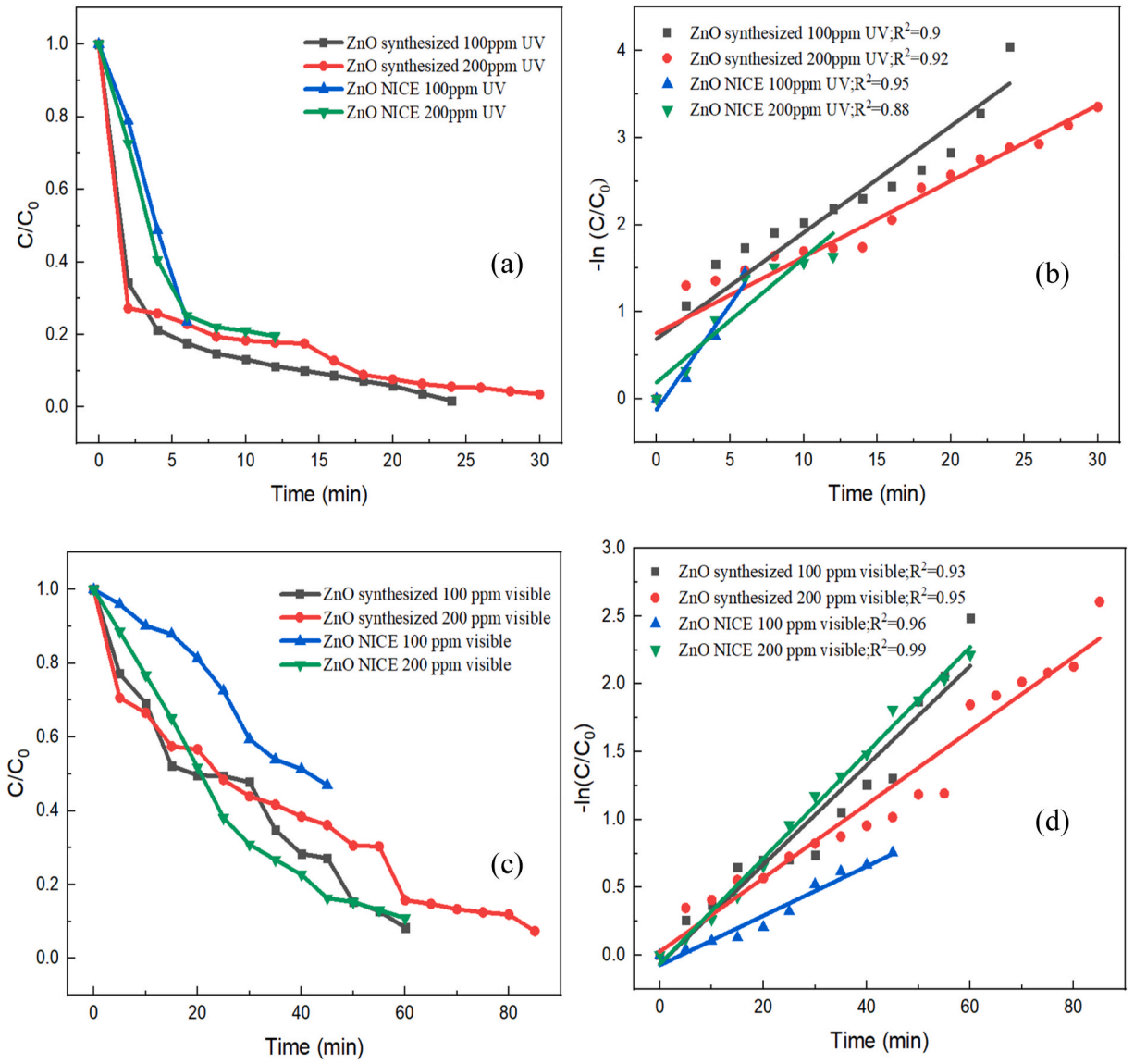

Fig. 11. Plot showing relation between (a) and (c) C/C_0, (b) and (d) $-\ln(C/C_0)$ versus reaction time for purchased and synthesized ZnO in reducing 100 and 200 ppm concentration of chromium solutions in UV and Visible light.

deterioration to 52 % after annealing at 800 °C, showing the loss of organic and volatile contents. Citing the EDX data, presence of 44 % of oxygen was quantified in ZnO even after annealing at 800 °C, hence the organo zinc complex made would be more oxygen rich. The defect induced by oxygen was also visible in the UV spectra, as the drop in energy band is ascribed to the interstitial defects of oxygen [41].

3.8. Photocatalytic activity

The photocatalytic activity of synthesized ZnO NP for Cr (VI) reduction was studied with two concentrations of 100 and 200 ppm under visible light from a Luker LED lamp (110 W), with a flux of 1190 and UV-C generated from Godrej SD VIROSHIELD 30UV. The reduction was followed using the DPC method, and the absorbance vs wavelength plot is shown in Fig. 9. The synthesized photocatalyst was compared with the purchased pristine ZnO to realise the real-world utility. The photocatalytic efficiency was evaluated by calculating reduction at specified intervals using the following equation (4) and is tabulated in Table 4.

$$\text{Percentage of reduction} = \frac{(A_I - A_F)}{A_I} \times 100 \quad (4)$$

A_I Initial absorbance.

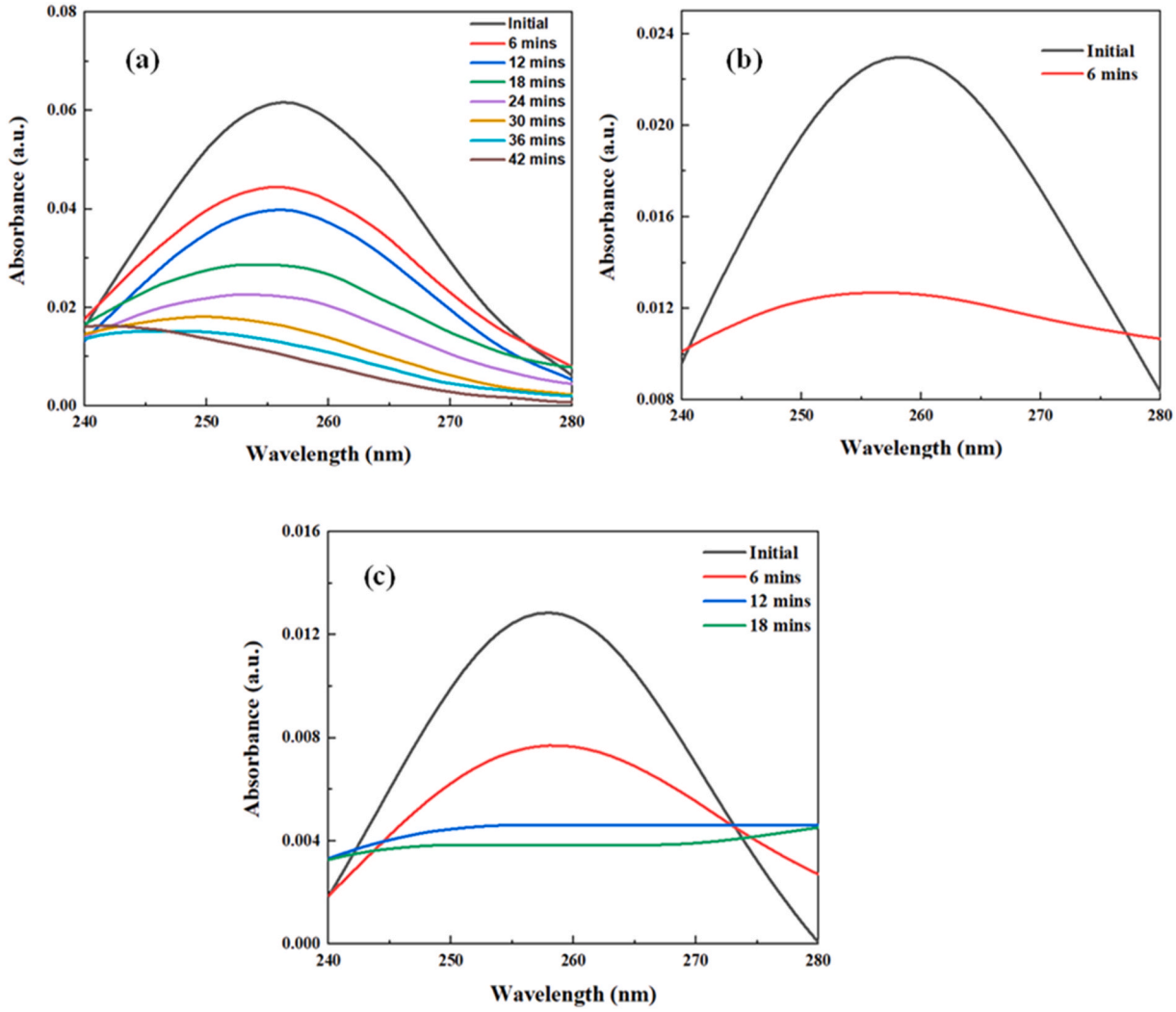

Fig. 12. Reduction in Sulphanilamide peak due to the photocatalytic activity of (a) synthesized ZnO, (b) NICE ZnO, and (c) reused ZnO.

Table 5
Percentage of degradation of sulphanilamide.

Photocatalyst	UV-C	
	Efficiency (%)	Time (min)
ZnO	84	42
ZnO (Nice)	44	6
ZnO Recycled	52	18

A_F - Final absorbance.

Table 4 reveals that both radiation sources were able to significantly decrease Cr (VI). It was found that UV-C radiation outperformed visible light in both 'time' and 'efficiency' to achieve a 99 % reduction for lower and higher concentrations of Cr (VI).

Table 4 shows that the synthesized ZnO was more efficient than the purchased ZnO. UV-C radiation eliminated 99.6 ppm and 198.2 ppm, while LED reduced 93 ppm and 184.2 ppm of Cr (VI) in 100 and 200 ppm concentrations. The corresponding narrow bandgap of 2.88 eV from the Tauc plot brings us to the conclusion that the UV radiation was able to reduce more than the visible light. Commonly observed defects like the oxygen vacancies in ZnO, introduce midgap state above the VB of ZnO, providing the trapping site for photoinduced electrons under irradiation. Thus, the recombination of photoinduced electron-hole pair under radiation can be critically retarded. Here, UV light reduced the recombination rate significantly compared to visible light, getting a potential degradation of 99 % [45]. Fig. 10 shows the reproducibility and stability of the catalyst used under UV and Visible radiation for 100 and 200 ppm

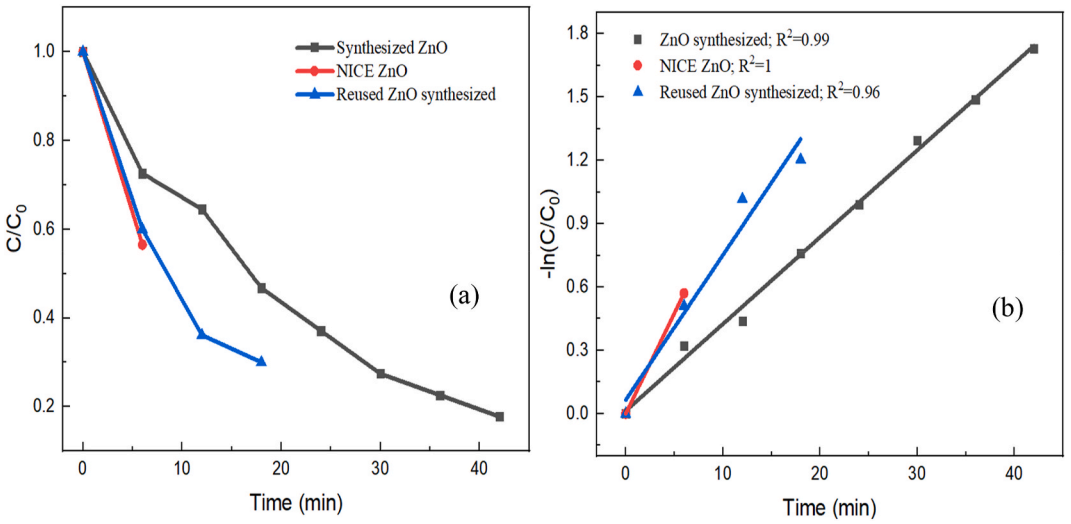

Fig. 13. Plot showing relation between (a) C/C_0 and (b) $-\ln(C/C_0)$ versus reaction time for synthesized, purchased and reused ZnO in degrading sulphanilamide drug.

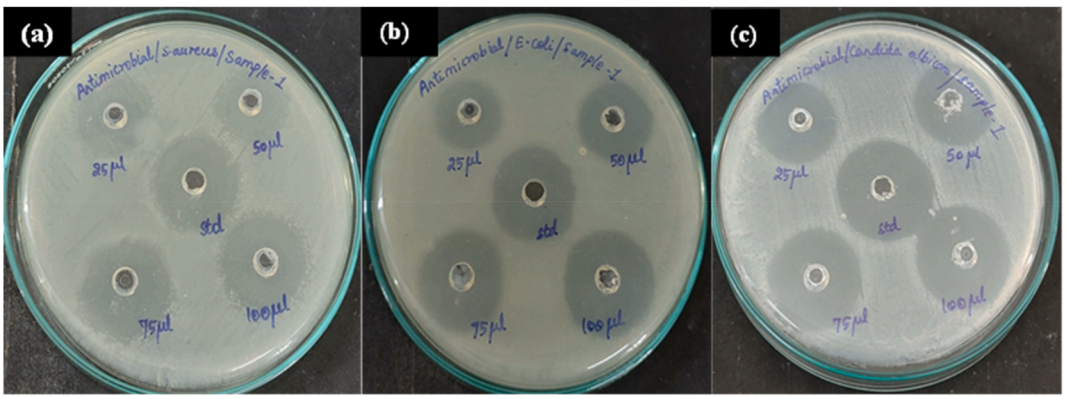

Fig. 14. Zone of inhibition at different concentration of ZnO synthesized (a) *S. aureus*, (b) *E. coli* and (c) *Candida albicans*.

Table 6
Antimicrobial activity with different concentrations of Chloramphenicol Fugues- Fluconazole as positive control.

Sl. No.	Strains	25 µL	50 µL	75 µL	100 µL
1	*S. aureus*	0.5 cm	0.5 cm	0.5 cm	0.5 cm
2	*E. Coli*	1.0 cm	1.0 cm	1.0 cm	1.0 cm
3	*Candida albicans*	1.0 cm	1.0 cm	1.0 cm	1.0 cm

Table 7
Antimicrobial activity with different concentrations of synthesized ZnO.

S.no	Strains	25 µl	50 µl	75 µl	100 µl
1	*S. aureus*	0.5 cm	0.6 cm	0.9 cm	1.0 cm
2	*E. Coli*	0.4 cm	0.5 cm	0.8 cm	1.1 cm
3	*Candida albicans*	0.5 cm	0.6 cm	1.1 cm	1.2 cm

concentrations of Cr (VI). It is checked for 5 operation cycles and found, after 5 cycles, the efficiency decreases from 99.6 to 99.1 % to 42.3 and 48.3 % under UV and from 92.1 to 93 % to 35.8 and 39.3 % under visible, respectively, for 100 and 200 ppm concentrations of Cr (VI) solution. It might be due to leaching of active metal sites from the catalyst and/or adsorption of reactants/products on the surface of the catalyst [46,47].

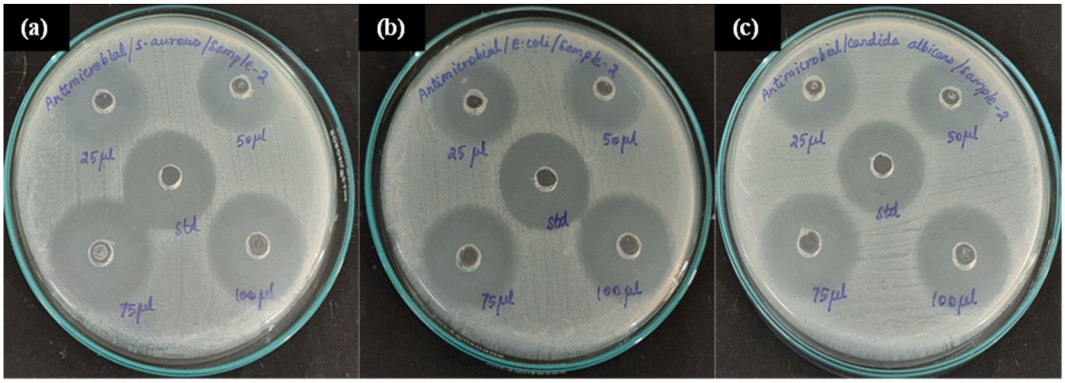

Fig. 15. Zone of inhibition at different concentration of organo zinc complex synthesized (a) *S. aureus*, (b) *E. Coli* and (c) *Candida albicans*.

Table 8
Antimicrobial activity with different concentrations of synthesized organo zinc complex.

Sl. No.	Strains	25 µL	50 µL	75 µL	100 µL
1	*S. aureus*	0.8 cm	0.9 cm	1.3 cm	1.2 cm
2	*E. Coli*	0.5 cm	0.4 cm	0.9 cm	1.2 cm
3	*Candida albicans*	0.7 cm	0.6 cm	1.0 cm	1.0 cm

The kinetics of Cr (VI) reduction onto ZnO obey a first-order reaction model given by equation (5) [48].

$$\ln\left(\frac{C}{C_0}\right) = K_{app}\, t \tag{5}$$

At the start and specific illumination times, C_o, and C (ppm) represent the initial and residual chromium concentrations. Fig. 11 displays the relationship along C/C_0 and -ln (C/C_0) versus reaction duration for 100 and 200 ppm concentrations of Cr (VI). Upon UV-C illumination, the rate constant of 100 and 200 ppm chromium solutions for synthesized and purchased ZnO were predicted to be 0.1221, 0.241 and 0.0873, 0.1361 min^{-1}, respectively. Upon LED illumination, the rate constants of 100 and 200 ppm chromium solutions for synthesized and purchased ZnO were predicted to be 0.0366, 0.0177 and 0.0272, 0.0376 min^{-1}, respectively. An explanation for the higher photocatalytic capability of ZnO nanoparticles might be the appropriate interaction which aids electron mobility and reduces electron-hole recombination [49].

The degradation efficiency of synthesized ZnO against sulphanilamide is shown in Fig. 12 using UV-C radiation.

The synthesized ZnO was able to degrade 84 % of the sulphanilamide present in 8.4 ppm solution and the percentage of degradation is calculated and tabulated in Table 5.

The kinetics of sulphanilamide degradation is also studied. Fig. 13 displays the relationship along C/C_0 and -ln (C/C_0) versus reaction duration. Upon UV-C illumination, the sulphanilamide degradation rate for synthesized, purchased, and reused ZnO were predicted to be 0.0411, 0.0951 and 0.0686 min^{-1}, respectively. An explanation for the higher photocatalytic capability of ZnO nanoparticle might be the appropriate interaction which aids electron mobility and reduces electron-hole recombination [49].

The activity of a freely accessible ZnO laboratory reagent acquired from NICE chemicals was used to confirm the validity of the described green synthesis technique. The same procedure was followed, using the NICE ZnO instead of the synthesized ZnO. When using the NICE ZnO the maximum degradation is obtained in 6 min. At the end of the 6th minute, the NICE ZnO could only degrade 44 % of the sulphanilamide as shown in Fig. 12. This indicates that the green synthesized ZnO outperformed ZnO (NICE).

The reusability of the synthesized ZnO for photocatalysis is one of the most important characteristics [50,51]. Therefore, the ZnO was reused for the degradation of sulphanilamide following the same condition. The maximum degradation of 52 % occurs at 18 min, as shown in Fig. 12. This shows that the same ZnO has the capability to be used as a photocatalyst for multiple degradation. The percentage of photodegradation using all these photocatalyst (Synthesized ZnO, NICE ZnO, ZnO reused) is given in Table 5. The entire procedure was repeated multiple times, to ensure that the data which was obtained during the photocatalysis was reproducible.

3.9. Antimicrobial activity of synthesized ZnO

The antibacterial activity and minimum inhibitory concentrations of plant extracts against Gram-positive and Gram-negative bacteria were determined using agar well diffusion method. Antimicrobial activity against three pathogens were carried out with Chloramphenicol Fugues - Fluconazole as positive control. At different concentrations, the ZnO synthesized is exhibiting different inhibition zone, Fig. 14, and Table 6.

As the concentration of sample increases the zone of inhibition (the region around which the bacteria are destroyed) is found to be increasing. From Table 7, it is evident that the synthesized ZnO at 75 µL and 100 µL has outperformed the inhibition zone of positive

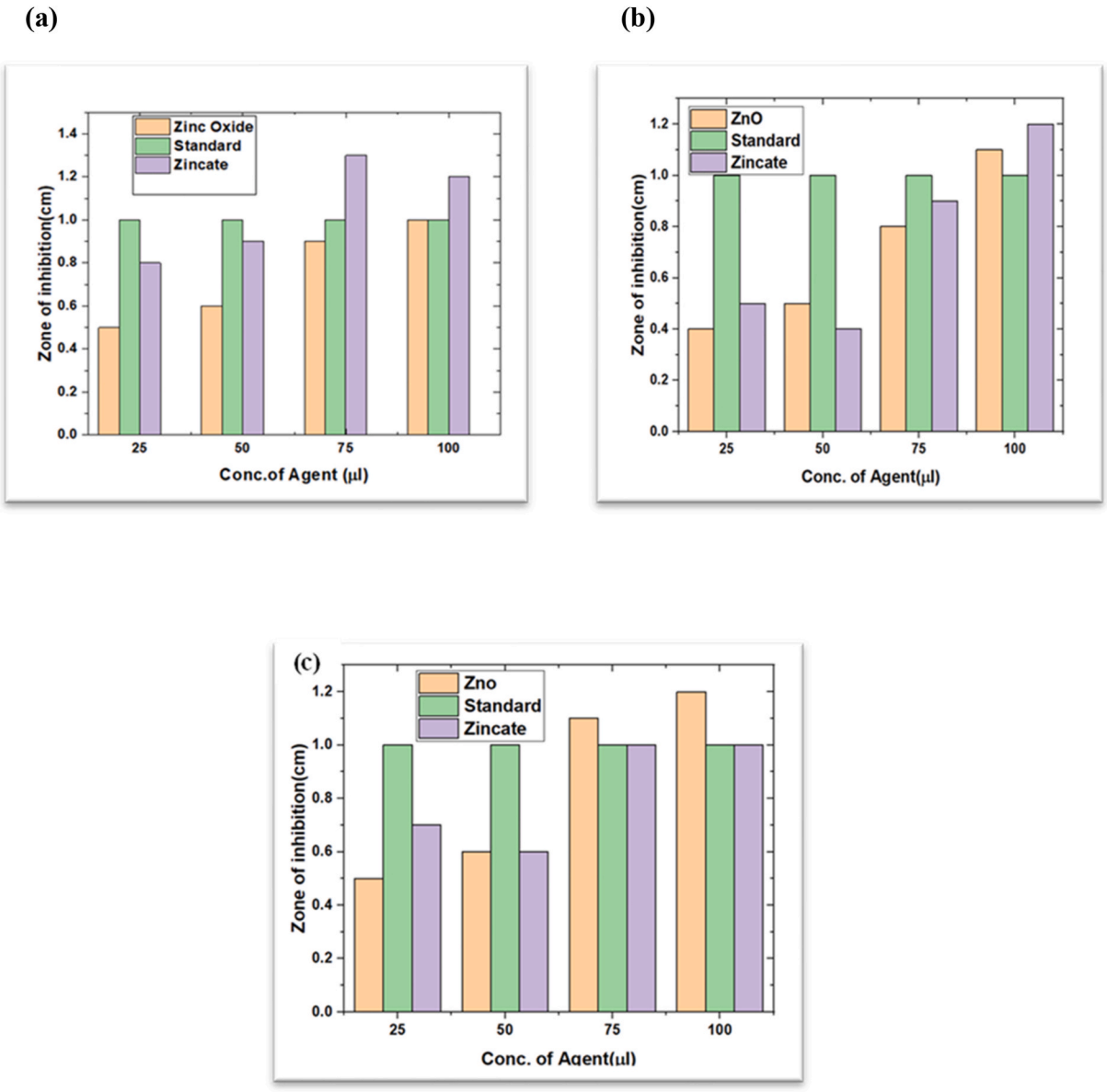

Fig. 16. Zone of inhibition (a) *S. aureus*, (b) *E. Coli* and (c) *Candida albicans*.

control used in inhibiting Candida albicans. At different concentrations, the organo zinc complex synthesized is exhibiting different inhibition zone, Fig. 15.

The zone of inhibition is shown to grow as sample concentration increases. Table 8 shows that the synthesized organo zinc complex at 75 and 100 µL surpassed the inhibition zone of the positive control in inhibiting S. aureus. For 75 and 100 µL, inhibiting activity equalled the positive control utilized in *Candida albicans*.

The performance of both synthesized samples was encouraging, and both ZnO and organo zinc complex potentially qualify as effective antibacterial agents, Fig. 16.

3.10. Cytotoxicity analysis of synthesized ZnO

For cytotoxicity testing, successive twofold dilutions from 100 µM to 0 µM were produced and employed for treatment. Half maximum inhibitory concentration (IC50) is a measure of compound's ability to impede biological or metabolic function. This quantitative measure reflects how much of certain medicine or other substance (inhibitor) is required to block by half a given biological process (or component of a process, such as an enzyme, cell, cell receptor, or microbe). Here in this study, we used MG-63 cell line to check the toxic potency of the synthesized samples, Fig. 17.

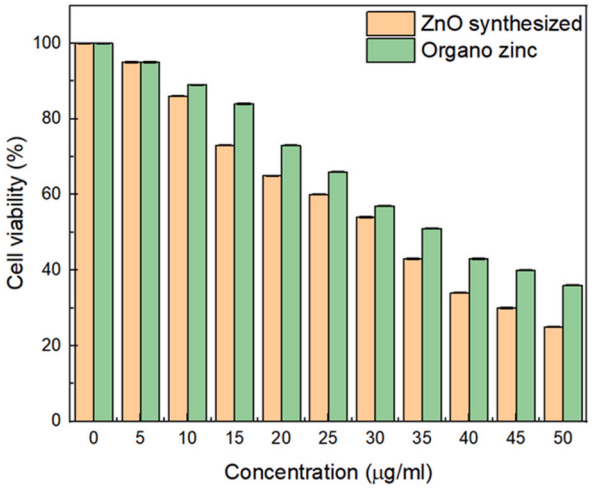

Fig. 17. Cell viability at different concentration of ZnO and organo zinc complex against MG-63 cell line.

It is evident from graph that the IC50 value for ZnO, organo zinc complex and cisplatin respectively are 34.36 ± 0.05, 37.25 ± 0.05, and 2.75 ± 0.05 µg/mL, which denote lesser toxic potency of synthesized nanoparticle. From Fig. 17, it is evident that cell viability reduces to 25 and 36 % for ZnO and organo zinc complex at high concentrations of 50 µg/mL. The maximum concentration of the samples in the limit of less toxic potency is 15 and 20 µg/mL for zinc oxide and organo zinc complex showing viability greater than 70 %. This shows our samples have better non-toxic potential compared to the cisplatin drug having a cell viability of only 14 % for just 10 µg/mL concentration. Fig. 18 illustrates the morphological changes and cell viability of MG-63 cells under different treatment conditions.

4. Conclusion and future scope

This work put forwarded a novel method of Piper Longum L assisted Zinc Oxide nanoparticle synthesis for the first time. The particle when tested for its activity, the green channel synthesized ZnO using Piper longum L has shown an edge above the performance of conventional ZnO. Structural and morphological analysis of the synthesized ZnO nanoparticle by XRD and SEM showed the confirmation and formation of ZnO nanorods. CHNS analysis was done to confirm the presence of organic moiety in the organo zinc complex formed. Phytochemical analysis confirmed presence of Alkaloids, Flavonoids, Glycosides, Phenols, Saponins, Sterols, and Tannins in the extract. The photocatalytic activity of the green synthesized ZnO showed higher efficiency with complete degradation of the Cr (VI) and sulphanilamide drug, in less time when compared to the conventionally synthesized ZnO. The magnetic property analyzed for both Zinc and organo zinc complex has shown remarkable magnetization saturation value in comparison with their counter parts, together with less toxic potential obtained for ZnO and organo zinc complex widens the scope of ZnO encapsulated drug delivery mechanism which is further sided by the small crystalline size of ZnO nanorods obtained. This effort would also place extract of Piper longum L as an alternative to CTAB in preventing agglomeration.

Bioavailability study of the obtained nanoparticle and a more detailed review of its cytotoxicity would better place the synthesis method adopted in this work of mine as a more nuanced way of obtaining ZnO NP which has the potency to outperform the activity of conventionally procured ZnO NP. Further studies on improving the non-cytotoxic potential of ZnO via biogenic route will be carried out. Sustainability in zinc oxide synthesis and its multifunctional application is effective in employing Piper longum L in a more pragmatic way than it has ever been previously. The study has broadened the reach of Piper Longum L, which will directly benefit Indian spice growers by increasing the value of their harvest.

Data availability statement

Questions	Response
Sharing research data helps other researchers evaluate your findings, build on your work and to increase trust in your article. We encourage all our authors to make as much of their data publicly available as reasonably possible. Please note that your response to the following questions regarding the public data availability and the reasons for potentially not making data available will be available alongside your article upon publication.	***Data will be made available on request.***
Has data associated with your study been deposited into a publicly available repository?	***No.***

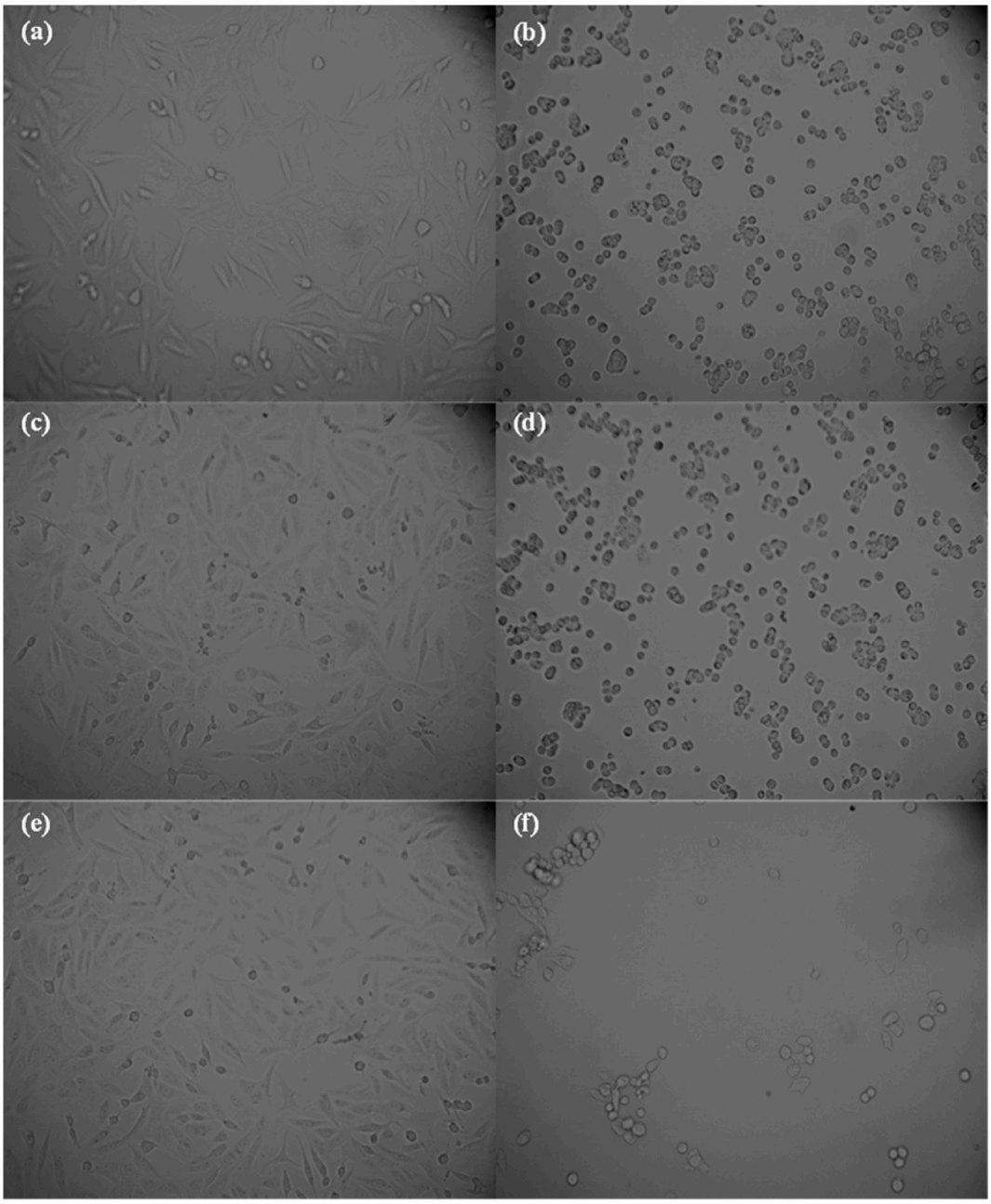

Fig. 18. (a) MG-63 cells-Control-ZnO (b) MG-63 cells-Treated-ZnO at 50 μg/mL (c) MG-63 cells-Control-organo zinc complex (d) MG-63 cells-Treated-organo zinc complex at 50 μg/mL (e) MG-63 cells-Control-Cisplatin (f) MG-63 cells-Treated-Cisplatin at 10 μg/mL.

Declaration of generative AI in scientific writing

During the preparation of this work the author(s) used ChatGPT4 in order to improve the readability and language. After using this tool/service, the author(s) reviewed and edited the content as needed and take(s) full responsibility for the content of the publication.

CRediT authorship contribution statement

Daphne Mary John: Writing – original draft, Validation, Methodology, Data curation. **Nilesh S. Pillai:** Methodology, Investigation, Formal analysis, Data curation. **Akshay Sivan:** Validation, Investigation, Formal analysis, Data curation. **Lasya P:** Visualization, Validation, Software, Methodology. **Archana P:** Visualization, Validation, Software, Methodology. **K.M. Sreekanth:** Writing –

review & editing, Supervision, Project administration, Investigation, Conceptualization. **Sivasubramanian G:** Writing – review & editing, Supervision, Resources, Conceptualization. **Sreedhar K.M:** Writing – review & editing, Validation, Supervision, Investigation.

Declaration of competing interest

The authors declare the following financial interests/personal relationships which may be considered as potential competing interests: G Sivasubramanian reports financial support was provided by Govt. of India Ministry of Science & Technology, Department of Science and Technology and Amrita Vishwa Vidyapeetham, India. If there are other authors, they declare that they have no known competing financial interests or personal relationships that could have appeared to influence the work reported in this paper.

Acknowledgements

The research grant provided by the Department of Science and Technology (DST), Government of India, under the reference DST/SEED/SUTRA/2020/232, is gratefully acknowledged by G. Sivasubramanian and Sreekanth K.M. We extend our heartfelt gratitude to 'AMMA', the Chancellor of Amrita Vishwa Vidyapeetham, for continual support and blessings. Our sincere thanks go to Dr. Senthil Kumar, Senior Technical Assistant at the Green Technologies Lab, Amrita Vishwa Vidyapeetham, Coimbatore Campus, for facilitating the use of the TGA, FESEM, and EDX characterization facilities. We also thank Mr. Manoj Prajapat, Lab Technician at the Indian Institute of Science, Education and Research, Bhopal, for providing access to the magnetic characterization facility. Appreciation is also due to the PSG Institute of Advanced Studies, Research, Innovation and Incubation Centre, Coimbatore, for their assistance with XRD characterization. Lastly, we acknowledge the contributions of VJ Biotech, Coimbatore, for their assistance in the antimicrobial studies and cytotoxicity analysis.

References

[1] A. Kołodziejczak-Radzimska, T. Jesionowski, Zinc oxide—from synthesis to application: a review, Materials 7 (4) (Apr. 2014) 2833–2881, https://doi.org/10.3390/ma7042833.
[2] D.K. Sharma, et al., A review on ZnO: fundamental properties and applications, Mater. Today: Proc. 49 (2022) 3028–3035, https://doi.org/10.1016/j.matpr.2020.10.238.
[3] N. Amal, et al., ZnO codoped with Si and Mn – preparation, characterization and photocatalytic reduction of hazardous chromium (VI) by the codoped ZnO, Mater. Today: Proc. 80 (Part 2) (2023) 947–951, https://doi.org/10.1016/j.matpr.2022.11.333. ISSN 2214-7853.
[4] Gautham, et al., Synthesis, structural and optical properties of Mn doped ZnO with its photocatalytic activity, Asian J. Chem. 30 (12) (2018) 2631–2637, https://doi.org/10.14233/ajchem.2018.21488.
[5] Malavika Menon, et al., ZnO and Mn-doped ZnO generated under three different synthesis conditions and photocatalytic reduction of hazardous hexavalent chromium by these photocatalysts, Mater. Today: Proc. 66 (Part 4) (2022) 2374–2380, https://doi.org/10.1016/j.matpr.2022.06.333. ISSN 2214-7853.
[6] U. Sachin Varma, et al., Co-precipitation as a tool for effective doping of magnesium in zinc oxide: studies on structural, optical and photocatalytic properties, Rasayan Journal of Chemistry 11 (2018) 1491–1500, https://doi.org/10.31788/RJC.2018.1144000.
[7] K.M. Sreedhar, et al., ZnO CO-DOPED WITH Ni AND Mg: PREPARATION BY COPRECIPITATION, CHARACTERISATION, AND EFFECT OF AMOUNT OF THE CO-DOPANTS ON THE BANDWIDTH OF ZnO, Rasayan Journal of Chemistry 14 (2021) 1289–1296, https://doi.org/10.31788/RJC.2021.1426031.
[8] A.M. Parameswaran, N.K. Amal Kaitheri, On the flash sintering behavior of Li: ZnO—evidence of electrode asymmetry driven by electrochemical reactions, J. Am. Ceram. Soc. 106 (2023) 6454–6468, https://doi.org/10.1111/jace.19295.
[9] D. Karthika, Sri Parvathy V. Varrier, P. Anand Mohan, A.K. Nanda Kumar, A structural and ac conductivity study on Li-doped ZnO, ECS Journal of Solid-State Science and Technology 10 (8) (2021) 081016. https://iopscience.iop.org/article/10.1149/2162-8777/ac1d24.
[10] Kahsay, et al., Green synthesis of zinc oxide nanostructures and investigation of their photocatalytic and bactericidal applications, RSC Adv. 9 (63) (2019) 36967–36981, https://doi.org/10.1039/C9RA07630A.
[11] J. Liu, et al., The toxicology of ion-shedding zinc oxide nanoparticles, Crit. Rev. Toxicol. 46 (4) (Apr. 2016) 348–384, https://doi.org/10.3109/10408444.2015.1137864.
[12] V.N. Kalpana, V. Devi Rajeswari, A Review on Green Synthesis, Biomedical Applications, and Toxicity Studies of ZnO NPs, Bioinorganic Chemistry and Applications (2018) 12, https://doi.org/10.1155/2018/3569758, 3569758.
[13] J. Arumugam, et al., Green synthesis of zinc oxide nanoparticles using Ficus carica leaf extract and their bactericidal and photocatalytic performance evaluation, Chem. Phys. Lett. 783 (2021) 139040, https://doi.org/10.1016/j.cplett.2021.139040. ISSN 0009-2614.
[14] N. Matinise, et al., ZnO nanoparticles via Moringa oleifera green synthesis: physical properties & mechanism of formation, Appl. Surf. Sci. 406 (2017) 339–347, https://doi.org/10.1016/j.apsusc.2017.01.219. ISSN 0169-4332.
[15] Jeevan Mathew Tharayil, Prakash Chinnaiyan, Biogenic synthesis of ZnO from Rubia cordifolia root extract: a study on sono-photocatalytic dye degradation and anti-bacterial assay, Results in Engineering 20 (2023) 101567, https://doi.org/10.1016/j.rineng.2023.101567. ISSN 2590-1230.
[16] Faisal, et al., Green synthesis of zinc oxide (ZnO) nanoparticles using aqueous fruit extracts of myristica fragrans: their characterizations and biological and environmental applications, ACS Omega 6 (14) (2021) 9709–9722, https://doi.org/10.1021/acsomega.1c00310.
[17] Sauvik Raha, Md Ahmaruzzaman, ZnO nanostructured materials and their potential applications: progress{,} challenges and perspectives, Nanoscale Adv. 4 (8) (2022) 1868–1925RSC, https://doi.org/10.1039/D1NA00880C.
[18] V. Yadav, et al., A systematic review on Piper longum L.: bridging traditional knowledge and pharmacological evidence for future translational research, J. Ethnopharmacol. 247 (Jan. 2020) 112255, https://doi.org/10.1016/j.jep.2019.112255.
[19] Min Hwang et al., " Determination of Essential and Toxic Elements in Vegetables from South Korea", Anal. Lett. 50, 663-681, https://doi.org/10.1080/00032719.2016.1194426.
[20] S. Asha, et al., Efficient photocatalytic degradation of industrial contaminants by Piper longum mediated ZnO nanoparticles, Environ. Res. 208 (2022) 112686, https://doi.org/10.1016/j.envres.2022.112686. ISSN 0013-9351.
[21] A. Teklay, Physiological effect of chromium exposure: a review, Int. J. Food Sci. Nutr. Diet. (Jun. 2016) 1–11, https://doi.org/10.19070/2326-3350-SI07001.
[22] C. Liao, et al., Interactions of zinc oxide nanostructures with mammalian cells: cytotoxicity and photocatalytic toxicity, Int. J. Mol. Sci. 21 (17) (Aug. 2020) 6305, https://doi.org/10.3390/ijms21176305.
[23] P.S. Kulkarni, et al., 1,5 diphenyl carbazide immobilized cross-linked chitosan films: an integrated approach towards enhanced removal of Cr(VI), J. Mol. Liq. 247 (Dec. 2017) 254–261, https://doi.org/10.1016/j.molliq.2017.09.122.
[24] S. Asha, et al., Efficient photocatalytic degradation of industrial contaminants by Piper longum mediated ZnO nanoparticles, Environ. Res. 208 (2022) 112686, https://doi.org/10.1016/j.envres.2022.112686.

[25] Anku, et al., Photocatalytic degradation of pharmaceuticals using graphene-based material, in: A New Generation Material Graphene: Applications in Water Technology, Springer, Cham, 2019, pp. 187–208.
[26] Khasawneh, et al., Photocatalytic degradation of pharmaceuticals using TiO based nanocomposite catalyst-review, Civ. Environ. Eng. Rep. 29 (3) (2019) 1–33.
[27] M. Yan, M.H. Majd, Evaluation of induced apoptosis by biosynthesized zinc oxide nanoparticles in MCF-7 breast cancer cells using Bak1 and bclx expression, Dokl. Biochem. Biophys. 500 (1) (Sep. 2021) 360–367, https://doi.org/10.1134/S1607672921050148.
[28] Ananthu C. Mohan, B. Renjanadevi, Preparation of zinc oxide nanoparticles and its characterization using scanning electron microscopy (SEM) and X-ray diffraction(XRD), Procedia Technology 24 (2016) 761–766, https://doi.org/10.1016/j.protcy.2016.05.078. ISSN 2212-0173.
[29] Dr Irfan Qasim, Dr Muhammad Mumtaz, Kashif Nadeem, Syed Shah, Zinc nanoparticles at intercrystallite sites of (Cu 0.5 Tl 0.5)Ba 2 Ca 3 Cu 4 O 12− δ superconductor, J. Nanomater. 2016 (2016) 1–6, https://doi.org/10.1155/2016/9781790.
[30] Y. Waseda, et al., X-Ray Diffraction Crystallography: Introduction, Examples and Solved Problems, Springer, Heidelberg [Germany] New York, 2011.
[31] K.D. Vernon-Parry, Scanning electron microscopy: an introduction, III-Vs Rev. 13 (4) (Jul. 2000) 40–44, https://doi.org/10.1016/S0961-1290(00)80006-X.
[32] H.-H. Perkampus, UV-VIS Spectroscopy and its Applications, 1992, https://doi.org/10.1007/978-3-642-77477-5 [Online]. Available:. (Accessed 5 June 2022).
[33] J.C. Russ, et al., Fundamentals of Energy Dispersive X-Ray Analysis: Butterworths Monographs in Materials, Elsevier Science, Kent, 2014 [Online], https://www.everand.com/book/282593092/Fundamentals-of-Energy-Dispersive-X-Ray-Analysis-Butterworths-Monographs-in-Materials. (Accessed 5 June 2022).
[34] B.H. Stuart, Infrared Spectroscopy: Fundamentals and Applications, J. Wiley & Sons, Chichester (Royaume Uni); Hoboken (N.J.), 2009.
[35] Morteza Zargar Shoushtari, et al., The size dependence of the magnetic properties of ZnO and Zn1-xNixO nanoparticles, Mater. Res. Bull. 88 (2017) 315–319, https://doi.org/10.1016/j.materresbull.2017.01.006. ISSN 0025-5408.
[36] Zarate, et al., Development of a novel scaffold of chitosan, Type IV collagen and integrin α3β1 as alternative scaffold for primary culture of podocytes, Appl. Sci. 8 (2018) 930, https://doi.org/10.3390/app8060930.
[37] Natàlia Dave, et al., Secondary structure components and properties of the melibiose permease from Escherichia coli: a fourier Transform infrared spectroscopy analysis, Biophys. J. 79 (2) (2000) 747–755, https://doi.org/10.1016/S0006-3495(00)76332-6. ISSN 0006-3495.
[38] B.M. Keyes, et al., Infrared spectroscopy of polycrystalline ZnO and ZnO:N thin films, J. Cryst. Growth 281 (2–4) (Aug. 2005) 297–302, https://doi.org/10.1016/j.jcrysgro.2005.04.053.
[39] D. Sharma, R. Jha, Transition metal (Co, Mn) co-doped ZnO nanoparticles: effect on structural and optical properties, J. Alloys Compd. 698 (Mar. 2017) 532–538, https://doi.org/10.1016/j.jallcom.2016.12.227.
[40] X. Zheng, et al., Oxygen vacancy enhanced room temperature ferromagnetism in Ar+ ion irradiated WO3 films, Ceram. Int. 47 (4) (Feb. 2021) 5091–5098, https://doi.org/10.1016/j.ceramint.2020.10.087.
[41] S. Vyazovkin, et al., Handbook of Thermal Analysis and Calorimetry: Recent Advances, Techniques, and Applications, 6, 2018.
[42] Islam, et al., Enhanced photocatalytic reduction of toxic Cr(VI) with Cu modified ZnO nanoparticles in presence of EDTA under UV illumination, SN Appl. Sci. 1 (2019) 1240, https://doi.org/10.1007/s42452-019-1282-x.
[43] Yang, et al., Photocatalytic reduction of chromium(VI) in aqueous solution using dye-sensitized nanoscale ZnO under visible light irradiation, J. Nanoparticle Res. 11 (2009) 221–230, https://doi.org/10.1007/s11051-008-9423-y.
[44] Mrunal V. Kangralkar, et al., Photocatalytic degradation of hexavalent chromium and different staining dyes by ZnO in aqueous medium under UV light, Environ. Nanotechnol. Monit. Manag. 16 (2021) 100508, https://doi.org/10.1016/j.enmm.2021.100508. ISSN 2215-1532.
[45] F. Al Marzouqi, et al., A green approach to the microwave-assisted synthesis of flower-like ZnO nanostructures for reduction of Cr(VI), Toxicol. Environ. Chem. 101 (1–2) (2019) 1–12, https://doi.org/10.1080/02772248.2019.1635602.
[46] Yang, et al., Metallic ion leaching from heterogeneous catalysts: an overlooked effect in the study of catalytic ozonation processes, Environ. Sci.: Water Res. Technol 3 (6) (2017) 1143–1151, https://doi.org/10.1039/C7EW00273D. RSC.
[47] Deska Lismawenning Puspitarum et al., "Photocatalytic mechanism and properties of recyclable hybrid magnetic/semiconductor nanocomposites synthesized via green route for organic dye degradation", Results in Materials 19 (2023) 100439 https://doi.org/10.1016/j.rinma.2023.100439. ISSN 2590-048X.
[48] Kołodziejczak-Radzimska, et al., Structural characterisation of ZnO particles obtained by the emulsion precipitation method, J. Nanomater. (2012). https://www.hindawi.com/journals/jnm/2012/656353/.
[49] A.A. Ismail, et al., Mesoporous ZnCr2O4 photocatalyst with highly distributed PtO nanoparticles for visible-light-induced photoreduction of nitrobenzene, Opt. Mater. 122 (2021) 111676.
[50] A.A. Ismail, et al., Highly efficient and accelerated photoreduction of nitrobenzene over visible-light-driven PtO@Cr2O3 nanocomposites, Surface. Interfac. 27 (2021) 101527.
[51] J. Ge, Y. Zhang, et al., Advanced Design and synthesis of composite photocatalysts for the remediation of wastewater: a review, Catalysts 9 (2) (Jan. 2019) 122, https://doi.org/10.3390/catal9020122.